Journal of Photochemistry and Photobiology A: Chemistry 215 (2010) 17–24

Contents lists available at ScienceDirect

Journal of Photochemistry and Photobiology A: Chemistry

journal homepage: www.elsevier.com/locate/jphotochem

Structural and photoluminescence characterization of mesoporous silicon-phosphates

Carmen Tiseanu[a,*], Vasile Parvulescu[b,*], Viorica Parvulescu[c], Elena Cotoi[b], Andre Gessner[d], Michael Kumke[d], Simion Simon[e], Florin Vasiliu[f]

[a] Laboratory of Solid-State Quantum Electronics, National Institute for Laser, Plasma and Radiation Physics, P.O. Box MG-36, RO 76900, Romania
[b] Department of Chemical Technology and Catalysis, University of Bucharest, 4–12 Regina Elisabeta Bvd., Bucharest 030016, Romania
[c] Laboratory of Catalysis and Surface Chemistry, Institute of Physical Chemistry "I.G. Murgulescu, 202 Splaiul Independentei Str., Bucharest, Romania
[d] Department of Physical Chemistry, Institute of Chemistry, University of Potsdam, Karl-Liebknecht-Str. 24-25, 14476 Potsdam-Golm, Germany
[e] Faculty of Physics, Institute for Interdisciplinary Experimental Research, Babes-Bolyai University, Mihail Kogalniceanu Str. No. 1, 400084 Cluj-Napoca, Romania
[f] Laboratory of Advanced Materials for Special Applications, National Institute of Materials Physics (INCDFM), Bucharest, P.O. Box MG-7, R-76900, Romania

ARTICLE INFO

Article history:
Received 26 March 2010
Received in revised form 3 June 2010
Accepted 16 July 2010
Available online 24 July 2010

Keywords:
Silicates
Phosphorous
Mesoporous materials
Luminescence
Lanthanides

ABSTRACT

Two different types of mesoporous silicon-phosphate supports using different surfactants (a mixture of $(CH_3)_3C_{13}H_{27}NBr$ with an organophosphorus coupling molecule ($HO\text{-}PO(i\text{-}C_3H_7)_2$) and with a co-surfactant ($(C_2H_5)_3(C_6H_5)PCl$), respectively) were synthesized. Trivalent europium (Eu) ions were immobilized via ion-exchange on these supports. The resulting materials were characterized using nitrogen adsorption isotherms at −196 °C, thermogravimetric analysis, SEM, TEM, FT-IR, PXRD, CP/MAS. $^{1}H^{29}Si$ and ^{31}P NMR, DR-UV–vis as well as steady-state and time-resolved photoluminescence spectroscopy. The results evidenced that the co-polymerization of silicon and phosphorous yielded a unique morphology in these materials. Following calcination at 450 and 900 °C europium-exchanged silicon-phosphates with great surface area (BET = 600–705 $m^2\ g^{-1}$) and 3.4 nm sized mesopores were obtained. The differences among the optical properties of the non-calcined europium materials such as the emission lifetimes, local environment at the europium sites or the relative contribution of the upper excited levels to the total photoluminescence were assigned to the surfactants used in the synthesis. Calcination of the silicon-phosphates at higher temperatures than 450 °C did not induce major changes in the structural properties; in contrast, photoluminescence properties of europium were markedly improved in terms of intensity and average lifetime.

1. Introduction

Silica based organic–inorganic hybrid materials offer a series of advantages that make them very attractive for applications due to the multipurpose and relatively facile chemistry, easy shaping and patterning, good mechanical integrity and excellent optical quality and luminescence properties [1–4]. Silicon phosphonates were reported as a new interesting class of organic–inorganic materials [5–9]. The organic phosphonate in silicas can influence the adsorption selectivity of these materials [6,7] and therefore offers a strong binding site for catalytic metal ions [8]. In addition, the choice of the phosphorous-containing modifier controls the type- and size-distribution of the pores. A narrow mesopore range was found for the phosphonic acid-modified silicas in contrast to a bi-modal distribution of micro- and mesopores found in polysilsesquioxane-modified materials [9,10]. Because phosphorylation modulates the activity and biologic functions of proteins [11] the incorporation of phosphorous compounds into silica networks can be thought for bioactive materials based applications [12]. Phosphoryl and phosphate groups were also studied in connection with their hydrogen bond properties [13,14]. Thus, it was found that the hydrogen bonding properties of the phosphoryl group was approximately 100-fold more effective than carbonyl group in a similar molecular structure [14].

Based on this state of the art we intended to investigate the superficial properties of a family of mesoporous silicon-phosphates prepared by using different surfactants. Thus, the interaction of these materials is expected to offer useful information in this sense. For such a purpose we selected the ion-exchange technique with trivalent europium (Eu) as the exchanged ions. The europium ion was introduced as luminescence probe to assess for both the structure and luminescence properties. The silicon-phosphates were obtained following a hydrothermal treatment under microwave

* Corresponding authors. Tel.: +40 21 4113987; fax: +40 21 4574610.
E-mail addresses: tiseanuc@yahoo.com (C. Tiseanu), v_parvulescu@yahoo.com (V. Parvulescu).

1010-6030/$ – see front matter © 2010 Elsevier B.V. All rights reserved.
doi:10.1016/j.jphotochem.2010.07.015

activation using two different surfactant mixtures, (a mixture of $(CH_3)_3C_{13}H_{27}NBr$ with an organophosphorus coupling molecule (HO-PO(i-$C_3H_7)_2$) and with a co-surfactant (($C_2H_5)_3(C_6H_5)PCl$), respectively). Structural and spectroscopic characterization of the samples were performed using nitrogen adsorption isotherms at −196 °C, thermogravimetric (TG) analysis, PXRD, CP/MAS ^1H, ^{29}Si and ^{31}P NMR, DR-UV–vis, FT-IR, SEM, TEM and luminescence spectroscopy. In-depth investigation of the structural and emission properties of the silicon-phosphate materials exchanged with europium ions is pursued in relation with the temperature treatment and the effects of the surfactant used in the synthesis.

2. Experimental details

2.1. Synthesis

Two types of silicon-phosphates were prepared. Type 1 was prepared starting from a mixture of $(CH_3)_3C_{13}H_{27}NBr$, as structure directing agent (S1), (S1 was prepared via quaternization of dimethyltridecylamine with CH_3Br following a typical procedure) and HO-PO(i-$C_3H_7)_2$ as organophosphorus coupling molecule (S2) in H_2O and decane in a molar ratio of S1:S2:H_2O:decane = 0.05:0.03:1:0.09. A solution of phosphoric acid (85%) was added to adjust pH 2. After 3 h of mixing, tetramethylorthosilicate (TMOS) was added under vigorous stirring (molar ratio SiO_2:S1 = 1:0.012).The resulting sol–gel mixture was loaded into a Teflon autoclave and exposed to microwave irradiation at 80 °C for 3 h. The obtained sample was denoted as OSP1. Type 2 was prepared using a similar procedure, but a starting mixture of $(CH_3)_3C_{13}H_{27}NBr$ (S1) with $(C_2H_5)_3(C_6H_5)PCl$ as co-surfactant (S2) in H_2O and decane. The molar ratio S1:S2:H_2O:decane was 0.05:0.09:1:0.09. The sample was denoted as OSP2. In both cases, the obtained products were separated by filtration and washed with bi-distilled water until the conductivity of the washing water was determined to be below 10 μS. Finally, the samples were dried under vacuum conditions for 12 h at 100 °C. Immobilization of Eu on the OSP1 and OSP2 supports was done via ion-exchange. A quantity of 1 g of dried sample (OSP1 or OSP2) was vigorously stirred in a 0.3 M Eu $(NO_3)_3$ solution. After stirring, the solid was separated via centrifugation, washed, and dried at 100 °C for 12 h. The obtained samples were denominated as Eu–OSP1 and Eu–OSP2, respectively. Calcination was pursued at 450 and 900 °C by heating the samples in air with a heating rate of 0.3 °C min^{-1}. Chemical composition of these samples was determined by atomic emission spectroscopy using a Plasma 40, PerkinElmer equipment after appropriate dissolution of the solid samples following calcination at 450 °C. Thus, OSP1 sample contains 35 wt% (Si) and 2.1 wt% (P) while OSP2 contains 39 wt% (Si) and 1.4 wt% (P), respectively. The presence of exchanged Eu in the supports was confirmed by chemical analysis via ICP-AES and DR-UV/vis spectroscopy. The chemical analysis indicated an amount of ca. 0.8 wt% of immobilized Eu ions in the two samples.

2.2. Material characterization

Structural characterization of the investigated samples was performed using nitrogen adsorption isotherms at −196 °C, thermogravimetric analysis, PXRD, DR-UV/vis, FT-IR, TEM and SEM microscopy. The specific surface area of the samples and their micro pore volume were determined from nitrogen adsorption isotherms. The isotherms were collected at −196 °C with a Micrometrics ASAP2020 instrument, after degassing the samples *in situ* at 120 °C for 5 h. Powder X-ray diffraction patterns (PXRD) were collected on a Siemens D-5000, using Cu Kα radiation (λ = 1.54050 Å) and quartz as an external standard. Fourier transform infrared spectra (FT-IR) were collected in a Nicolet 4700 FT-IR instrument using the KBr pellet technique DR-UV/vis spectra were recorded with a Specord250 (Analytik Jena). Scanning electron microscopy (SEM) was performed using a Philips XL-20 microscope. Bright (BF) field images (TEM) of the porous aggregated particle systems were obtained with a JEOL 200 CX equipment working at an acceleration voltage of 200 kV. CP/MAS ^1H, ^{29}Si and ^{31}P NMR spectra were collected with a Bruker Avance 400 MHz spectrometer at room temperature, using a 4 mm double resonance probe head. The sample holder was spun with a frequency up to 15 kHz. Tetramethylsilane (TMS) and 85% H_3PO_4 were used as references for the chemical shift of the ^1H, ^{29}Si and ^{31}P signals, respectively.

2.3. Photoluminescence (PL) measurements

All PL measurements were performed at room temperature (20 °C). Time-resolved emission spectra (TRES) were recorded using a wavelength tunable Nd:YAG-laser/OPO system (Spectra Physics/GWU) operated at 20 Hz as excitation light source and an intensified CCD camera (Andor Technology) coupled to a spectrograph (MS257 Model 77700A, Oriel Instruments) as detection system. The TRES were collected using the box car technique. In a typical experiment the sample was non-selectively excited at λ_{ex} = 394 nm. The initial gate delay δt (delay after laser pulse) was set to two μs and the gate width Δt was adjusted to 50 μs. The PL was detected in the spectral range of 500 nm < λ_{em} < 750 nm with a spectral resolution of up to 0.08 nm. PL decays were also measured by using the "decay by delay" feature of the phosphorescence mode of the Fluoromax 4 spectrofluorometer (Jobin Yvon). The repetition rate of the flash lamp was 25 Hz, the integration window Δt varied between 300 ms and 1 s, the delay after flash δt was set between 0.05 and 1 ms and up to 75 flashes were accumulated per data point. The slits were set from 0.1 nm to 5 nm bandwidth in excitation as well as emission. The PL decay was measured by monitoring the decay at 614 nm corresponding to the maximum intensity of the emission spectrum. The PL decays were fitted with a multi-exponential function $f(t)$ using a commercial software (Origin, version 7.1):

$$f(t) = \sum_{i=1}^{n} A_i \exp\left(-\frac{t}{\tau_i}\right) + B \quad (1)$$

where A_i is the decay amplitude, B is a constant (the baseline offset) and τ_i is the time constant of the decay i. The average decay times were calculated using the following formula:

$$\langle\tau\rangle = \frac{\sum_{i=1}^{n} A_i \tau_i}{\sum_{i=1}^{n} A_i} \quad (2)$$

PL decay times τ (uncertainty ≤10%) given in Table 2 are the average values from at least five separate measurements.

3. Results and discussion

3.1. Characterization

3.1.1. Adsorption–desorption isotherms, thermogravimetry measurements and heat flow curves

The adsorption–desorption isotherms of nitrogen at −196 °C for the investigated samples are shown in Figure S1 in the supplementary data. For the dried samples (OSP1 and OSP2) a specific surface area of ca. 9 m^2 g^{-1} was determined. The BET isotherms supported the mesoporous character of the prepared samples. This small value is not related to any structure collapse, but to the fact that for the non-calcined materials the pores are still filled with the surfactant. After calcination at 450 °C both, surface area and pore volume,

Table 1
Textural characterization of Eu–OSP1 and Eu–OSP2.

Sample	BET surface area ($m^2\ g^{-1}$)	*t*-Plot surface area ($m^2\ g^{-1}$)	Average pore size (nm)	Pore volume ($cm^3\ g^{-1}$)
Dried OSP1	10	–	–	–
Dried Eu–OSP1	9	–	–	–
Calcined OSP1 (450 °C)	667	554	4.0	0.19
Calcined Eu–OSP1 (450 °C)	648	542	4.0	0.18
Calcined Eu–OSP1 (900 °C)	642	535	4.0	0.18
Dried OSP2	10	–	–	–
Dried Eu–OSP2	9	–	–	–
Calcined OSP2 (450 °C)	718	594	3.4	0.31
Calcined Eu–OSP2 (450 °C)	705	583	3.4	0.29
Calcined Eu–OSP2 (900 °C)	691	575	3.4	0.29

increased significantly for both the OSP1 and OSP2 supports. Differences between the two supports concerning surface area and pore volume are shown in Table 1. According to these data, calcination of the samples at higher temperatures than 450 °C was leading only to slight changes.

TG measurements and heat flow curves corresponding to the investigated samples show that both kinds of mixture surfactants were practically decomposed at 450 °C (curves not shown) and thus surface area and pore sized were increased. The differences between the composition of OSP1 and OSP2 were reflected by slight differences in the position of the peak maximums of the heat flow curves.

3.1.2. SEM analysis

SEM pictures of the investigated catalysts (Fig. 1) measured after the different stages of treatment confirmed the stability of the materials and the morphologies. These properties were well preserved even after calcination at 900 °C which is not unusual for a silicious material. Schemes S1 and S2 illustrate the interactions occurring in the synthesis of Eu–OSP1 and Eu–OSP2 samples. The formation of macropores, as a result of the surfactants association in the presence of decane, is confirmed by SEM microscopy. According to the SEM images, a low effect of surfactant and calcination on the morphology and dimension of macropores has been evidenced. The formation and morphologies of surfactant-silicate mesostructures are shaped by three processes [15]: (i) multidentate binding of silicate oligomers to the cationic surfactant, (ii) preferential silicate polymerization in the interface region, and (iii) the charge density matching between the surfactant and the silicate. The images suggest that the co-polymerization of silicon and phosphorus in aqueous phase ordered by surfactants leads to solids with a specific morphology. The mixture of two typical ionic surfactants and their high molar corresponded to a higher surface area and pore volume of OSP2 compared to OSP1. On the other side, OSP1 obtained with a mixture of a cationic (S1) and anionic (S2) surfactants corresponds to a more compact solid and to larger pores. In this case the interaction of the two surfactants is leading to larger aggregates around the non-polar phase (decane) (Table 1).

3.1.3. TEM analysis

TEM analysis provided additional information on the texture of these samples following calcination at 450 °C (Figure S2(a, b) in the supplementary data). Sample OSP1 calcined at 450 °C shows a very porous material with pores with diameters in the range 4–7 nm that is in a very good agreement with the values determined from the adsorption–desorption isotherms (Table 1). The TEM images for both supports reveal disordered morphology, close to wormhole-like pore morphology. However, compared with OSP1, the pores of OSP2 seem to be slightly smaller and have a higher density in agreement with data give in Table 1. This might correspond to the larger pore volume determined for this sample from the adsorption–desorption measurements.

3.1.4. PXRD patterns

As expected, the PXRD patterns indicate that these materials have an amorphous nature (Fig. 2). Calcination is not inducing additional forces that can order such structures. The random organization of the pores, in a good concordance with the wormhole-like pore structure shown in TEM images, can also been seen in the XRD patterns in the range 1–10° 2θ that is in line with data reported by other authors [5]. Similar PXRD patters were obtained, regardless the treatment temperature or sample.

SEM analysis of the europium-exchanged samples showed that the immobilization of the lanthanides did not cause any change in the morphology. The XRD measurements were in line with the SEM investigations with no changes observed in the XRD patterns after Eu immobilization.

3.1.5. NMR spectra

The solid state NMR investigation of the OSP1 and OSP2 samples indicated major differences among non-calcined and calcined samples (Fig. 3). The spectra deconvolution was made employing the Dmfit program. [16] The identified structural units are presented in Tables S1 and S2 in the supplementary data. The well-known Q^n notation was used for the PO_4 units, where n represents the number of oxygen atoms from the phosphorus first coordination sphere which link together two PO_4 tetrahedra [16]. For the dried samples ^{31}P CP/MAS NMR spectra displayed several Q^0_x lines (where x gives the number of the Q^0 line) which occur most probably due to a sample hydration effect, namely, to remnant humidity after drying (Fig. 3) [17–19]. In contrast to the calcined samples, the spectra of the dried Eu–OSP1 showed an additional Q^0_4 line (Table S1). For the dried Eu–OSP2 sample the additional lines were Q^0_1 and Q^0_2 (Table S2).

In order to certify the influence of the humidity on the material structure, the presence of hydrogen in the close proximity of the phosphorus environment was checked by ^1H–^{31}P CP/MAS NMR experiments with both dried and calcined samples [20]. The ^1H–^{31}P CP MAS NMR spectra of the dried Eu–OSP1 sample presents the maximum at the same isotropic chemical shift as the Q^0_4 unit (Fig. 3a). This proves that part of the hydrogen is placed nearby the Q^0_4 units, most probably as OH groups. In the case of the dried Eu–OSP2 sample, the ^1H–^{31}P CP MAS NMR spectra present a broad line covering the isotropic chemical shift of the lines corresponding to Q^0_1 and Q^0_2 units, confirming that these units have also hydrogen in their neighborhood (Fig. 3b). In addition, the NMR results showed that the other Q^n units have no hydrogen in their surrounding. The ^{31}P CP/MAS NMR spectra of the calcined samples indicated that the Q^n units without hydrogen in their surrounding were preserved. While in the case of the calcined Eu–OSP1 sample the majority PO_4 units are of Q^0 type, in the calcined Eu–OSP2 sample the majority of the PO_4 units has one P–O–P bond (Q_1). This in a perfect agreement with the model of the interactions occurring during the synthesis of these materials proposed in Schemes S1 and S2. ^{29}Si CP/MAS NMR spectra of calcined OSP1 and OSP2 samples show a rather small population of the Q_4-type Si-species that may account for the sur-

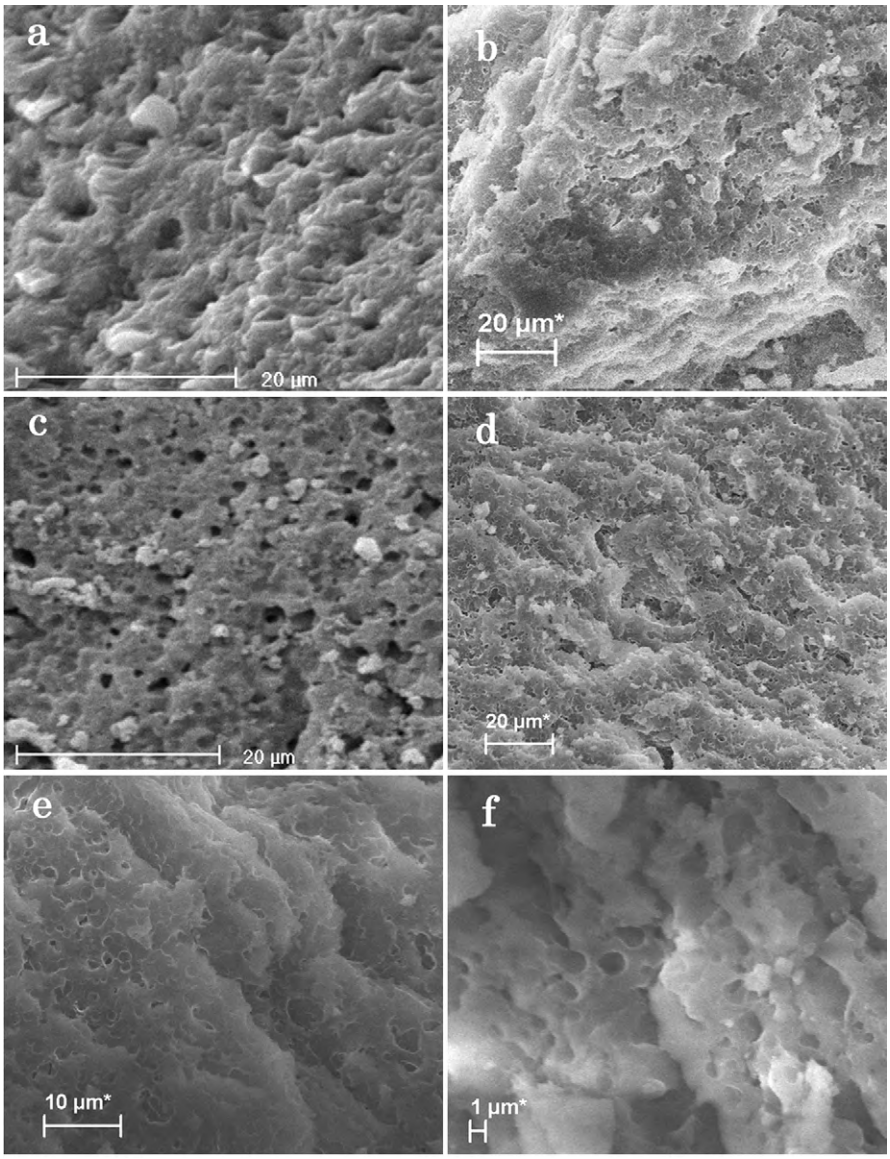

Fig. 1. SEM pictures of the SEM images of the as-synthesized (a) and calcined at 900 °C (b) Eu–OSP2; SEM images of the as-synthesized (c) and calcined at 900 °C (d) Eu–OSP1; SEM images with details on morphology for Eu–OSP1 calcined at 900 °C (e, f).

factant effect in the synthesis of these materials (see also Fig. 3c and Table S3 in the Supporting Information).

The population of the Q_4 species is higher for the Eu–OSP1 sample compared with Eu–OSP2. That may indicate an increased degree of polymerization of silica for this material which is in a way correlated with the degree of dimerization of phosphorus (see also the ^{31}P CP/MAS NMR spectra). The characterization methodology confirmed the fact phosphorus has been indeed inserted in the surfactant micelles via association of the ammonium quaternary salt with the surfactant containing phosphorus. The reason for which we have used the different phosphorus containing surfactants was directly connected to the size of the pores (Table 1). The anionic surfactant was leading to an increase of the micelle (which was a direct consequence of the pore size) via the formation of the poorer electronic species like $(OC_2H_5)_3Si^{2+}$ during the hydrolysis of alkoxide. In conclusion, the structural and textural characterization parameters obtained for these samples correspond to amorphous materials with mesoporous properties in which phosphor is present as Q_0 or Q_1 units (see also Schemes S1 and S2). According to this model these phosphorus species may constitute ion-exchange positions.

3.1.6. FT-IR data

Figure S3 shows the FT-IR spectra of the Eu–OSP1 and Eu–OSP2 samples compared with the pure OSP1 and OSP2 supports. Materials without europium present a band around 973 cm^{-1} which may be assigned to the formation of the P–OH bonds. The exchange of these materials with Eu led to the appearance of new bands at 919–923 cm^{-1} and 994–995 cm^{-1} which according with the literature data correspond to the formation of P–O–Eu bonds [21]. In addition, the band located at 1340 cm^{-1} provided evidence for the formation of the Si–O–P bonds [22].

3.2. Optical properties

3.2.1. Absorption and photoluminescence excitation spectra

Fig. 4 shows the DR-UV/vis as well as the PL excitation spectra of the Eu–OSP2. The f–f absorption transitions of europium are barely observable with the DR-UV/vis spectra. According to the PL excitation spectra the f–f transitions of Eu arising from the fundamental and thermally populated $^7F_0$ and $^7F_1$ levels are superimposed on a large absorption band centered at about 370 nm (dried sample). The broad band was tentatively assigned to the charge-

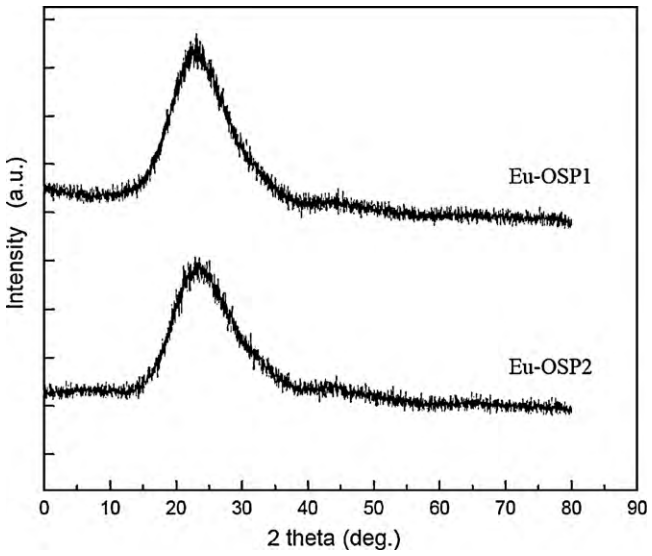

Fig. 2. PXRD patterns of Eu–OSP1 and Eu–OSP2 calcined at 450 °C.

transfer (CT) band of europium. The most intense f–f absorption of europium corresponds to the $^7F_0$–$^5L_6$ transition at 394 nm which was used as excitation wavelength in the steady-state as well as time-resolved photoluminescence measurements. Less intense f–f transitions were observed at about 464 nm ($^7F_0$–$^5D_2$ transition) or 520–540 nm ($^7F_{0,1}$–$^5D_1$ transitions). With increasing sample treatment temperature, the intensity of the CT transfer band is markedly decreased and narrowed being shifted toward smaller wavelengths (see also Figure S4 in the supplementary data). For the sample calcined at 900 °C, the CT band is centered at about 290 nm.

Similar behaviour of the DR-UV/vis spectra was obtained with Eu–OSP1 samples except for the slight differences observed for the case of dried samples. It is established that the peak position of the CT band of europium in various oxide materials depends on both the Eu–O bond length and the coordination environment [23,24]. Accordingly, the small differences between the dried Eu–OSP1 and Eu–OSP2 indicate the effects of the surfactant on the europium environments. After calcination at 900 °C the absorption maximum is located at 290 nm in both materials, showing that the nature of the europium species is not anymore controlled by the characteristics of the silicon-phosphate. The spectral shift observed in the spectra collected for the samples calcined at 900 °C compared with those dried or calcined at 450 °C accounts for a certain agglomeration of the Eu species with the increase of the temperature. The DR-UV/Vis spectra shows also an absorption at about 250 nm which increases with calcination temperature. This band was related to the support only (OSP1 or OSP2) being responsible for a broad short-lived luminescence peaked at 400 nm (see below).

3.2.2. Time-resolved photoluminescence spectra and excited-state dynamics

The time-resolved PL spectra (TRES) of the dried Eu–OSP1 and Eu–OSP2 samples following laser excitation at λ_{ex} = 394 nm are shown in Fig. 5. The PL spectra are composed of the characteristic Eu transitions centered at about λ_{em} = 579 nm ($^5D_0$–$^7F_0$), 590 nm ($^5D_0$–$^7F_1$), 614 nm ($^5D_0$–$^7F_2$), 653 nm ($^5D_0$–$^7F_3$) and 702 nm ($^5D_0$–$^7F_4$). The $^5D_1$ related emission with a lifetime of a few μs was also detected for both samples. At short delay after the laser pulse, δt = 2 μs, the intensity of the $^5D_1$ emission accounts for almost 25% of the total emission in Eu–OSP2 compared to only 10% in case of Eu–OSP1. The different non-radiative relaxation paths of this emission in the two samples may be assigned to the different surfactants used in the synthesis of the two samples.

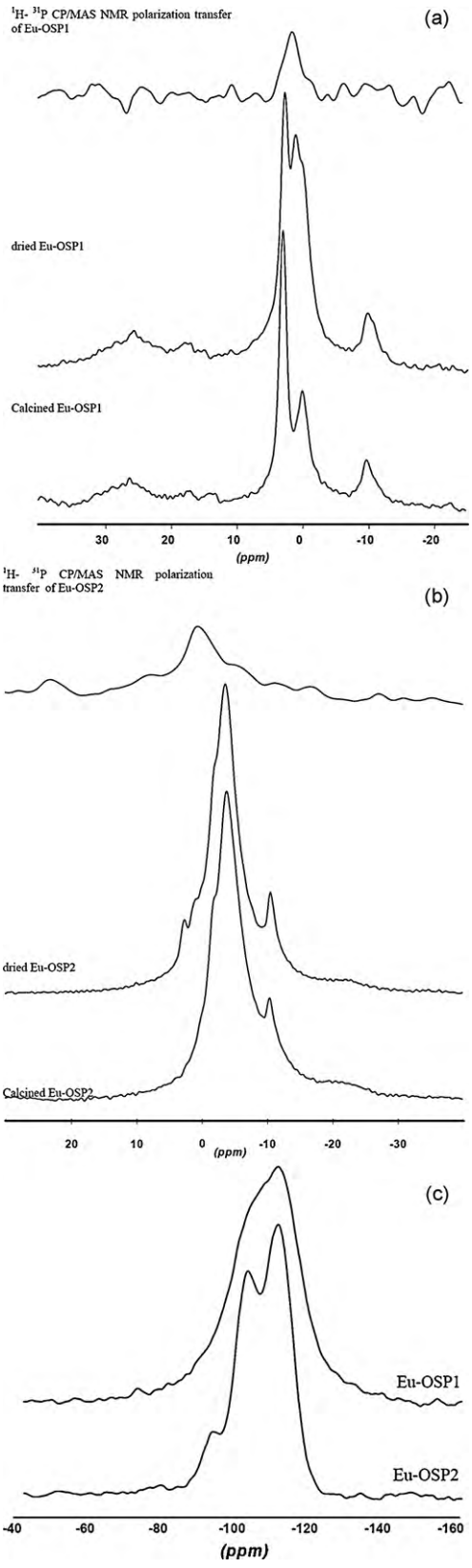

Fig. 3. (a) ^{31}P CP/MAS NMR spectra of Eu–OSP1; (b) ^{31}P CP/MAS NMR spectra of Eu–OSP2; (c) ^{29}Si CP/MAS NMR spectra of Eu–OSP1 and Eu–OSP2 calcined at 450 °C.

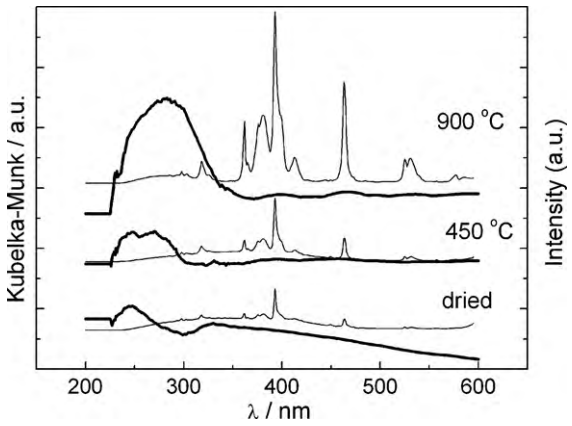

Fig. 4. DR-UV/vis (bold lines) and PL excitation (thin lines) spectra of Eu–OSP2 measured at λ_{em} = 614 nm.

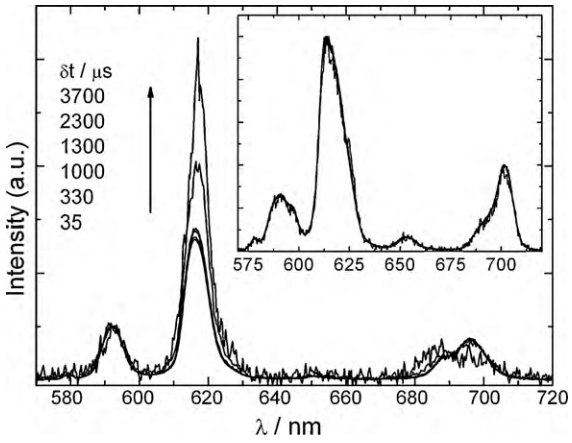

Fig. 6. Time-resolved PL spectra of dried and calcined (450 °C). Inset: Europium–OSP1 measured at various time delays (δt) after the laser pulse.

Steady-state PL spectra display, besides the characteristic europium emission, a broad (FWHM = 60 nm) short-lived emission peaked at 400 nm for all samples for excitation wavelengths 240 nm < λ_{ex} < 290 nm (Figure S5). The corresponding excitation spectra were peaked at about 250 nm which is also observed in all DR-UV/vis spectra (Fig. 4). With increasing treatment temperature, the ratio of the integrated intensity of the broad emission relative to that corresponding to the intraconfigurational 4f–4f Eu emission increased from about 1.6 for the dried samples to about 2.5 at 900 °C. To decide whether this emission is related to the $4f^6 5d^1 \rightarrow 4f^7 5d^0$ emission of the Eu^{2+} or the support, the emission of the un-doped supports OSP1 and OSP2 following excitation at ~250 nm was measured. The occurrence of the 400 nm centered emission confirmed its support-related origin.

The observation of the forbidden $^5D_0$–$^7F_0$ transition at λ_{em} = 579 nm indicates that Eu is located in low symmetry sites (C_{2v} or less) [25,26] in both OSP1 and OSP2 materials. Due to the electric and magnetic dipolar nature of the $^5D_0$–$^7F_2$ and $^5D_0$–$^7F_1$ transitions, respectively, the intensity ratio (asymmetry ratio, R) of the two transitions is used as an indicator of the local asymmetry and degree of covalency of the Eu bonding environment [27].

The asymmetry (R) values support a distorted environment at the europium sites, with more asymmetric europium coordination in Eu–OSP1 compared to Eu–OSP2. This may be explained by a more distorted oxygen environment induced by the mixture of the cationic and anionic surfactants at the exchange positions for europium (see also Schemes S1 and S2 in the supplementary data).

Following the calcination of Eu–OSP1 and Eu–OSP2 at 450 and 900 °C, the PL spectra of both materials were broadened. The peak maxima of the emission shifted to the blue ($^5D_0$–$^7F_1$, $^5D_0$–$^7F_2$) or red ($^5D_0$–$^7F_3$ and $^5D_0$–$^7F_4$) spectral region relative to the values measured for the dried samples. The asymmetry values, R of Eu–OSP1 and Eu–OSP2 show a similar increase with calcination temperature, about 4. 1 at 450 °C or 4. 4 at 900 °C. These effects are assigned to the OH removal from the first coordination sphere of europium with subsequent modification of the crystal-field at the europium sites. The intensity of the $^5D_0$–$^7F_4$ increased relative to the $^5D_0$–$^7F_1$ transition by a factor of 1.4–1.5 in the calcined samples (450 °C). Because the oscillator strength of the $^5D_0$–$^7F_4$ transition is attributed to bulk properties, such effect might support the long-range effects induced by calcination [27]. In addition, the $^5D_1$ emission was quenched in both supports (see inset of Fig. 5). In contrast with the $^5D_0$, the $^5D_1$ level provides a cross relaxation pathway of the europium emission via the Eu–Eu interactions [28] therefore the absence of this emission in the calcined samples may support for the europium clustering which was already speculated with the DR-UV/vis spectra (Fig. 4).

Further differences between dried and calcined Eu–OSP1 and Eu–OSP2 in terms of the spectral dynamics of europium PL are shown in Figs. 6 and 7.

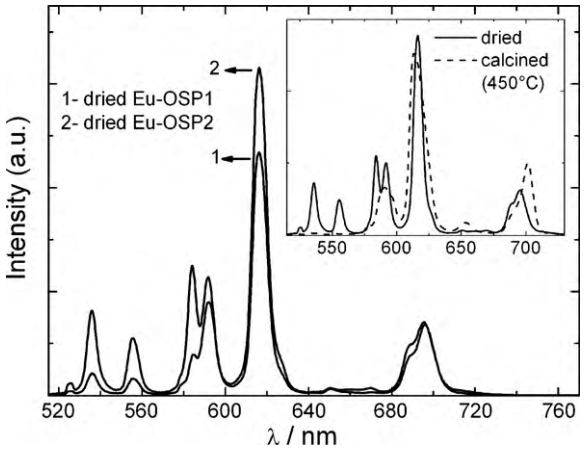

Fig. 5. Comparison between PL spectra of the dried europium–OSP1 and europium–OSP2 following laser excitation at 394 nm. Inset: the PL spectra for the dried and calcined Eu–OSP2 (450 °C). All spectra were measured at time delay, δt = 2 μs after the laser pulse and normalized to the intensity of $^5D_0$–$^7F_1$ transition. Spectra for the dried samples were normalized to the intensity of $^5D_0$–$^7F_1$ transition after the $^5D_1$ related emission was extracted from the total emission.

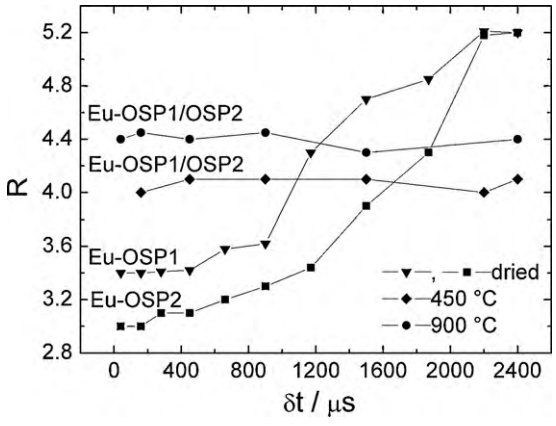

Fig. 7. Evolution with time delay after the laser pulse (δt) of the asymmetry ratio, R, for the Eu–OSP1 and Eu–OSP2. Thermal treatment is indicated on the figure. The initial delay was set to 30 μs for the dried Eu–OSP1 and Eu–OSP2.

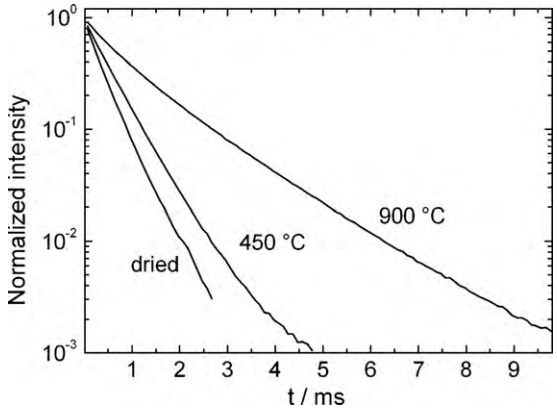

Fig. 8. PL decays of Eu–OSP1 following thermal treatment (λ_{ex} = 394 nm, λ_{em} = 614 nm).

It is well-known that the $^5D_0$–$^7F_0$ transition is a useful diagnostic tool for determining the number of Eu sites, i.e. there is one-to-one correspondence between the number of peaks associated with this transition in the emission spectrum and the number of distinct europium environments. For disordered solids like amorphous silica, multiple peaks can rarely be distinguished due to the inhomogeneous broadening effects. Instead, we have recently shown that the time-resolved luminescence spectra may be useful tool for assessing the distribution of europium species in various mesoporous materials [29]. Thus, for Eu in one chemical environment or single average Eu species, the asymmetry ratio R is expected to remain constant with time delay δt measured after the laser pulse, In contrast, for a system with a discrete or continuous distribution of luminescent Eu species, R becomes time dependent. According to Fig. 7, the R value obtained from the TRES of the dried samples are time delay-dependent, while upon calcination the TRES can be assumed constant, irrespective the support. The evolution of the TRES and the non-exponential PL decays shown in Figs. 6 and 8, respectively, can be explained by the existence of a europium species distributed on a large distribution of environments. The longest-lived europium has a small contribution (less than 10–15% of the total amplitude) and a highly distorted environment (R = 5.2). For the calcined samples (450 and 900 °C) the time evolution of R depicted in Fig. 7 point to a single average europium species for the dried samples.

3.2.3. *Excited-state dynamics and intrinsic quantum yields of emission*

The europium PL decays measured at λ_{em} = 614 nm are non-exponential (Fig. 8), regardless the support or treatment and were satisfactorily fitted by using two up to three exponentials (Eq. (1)). The departure of the europium PL decays from a single exponential observed for the calcined simple can result from europium ions with a distribution of closely related temporal properties. The average PL decay times calculated with Eq. (2) are listed in Table 2.

The average lifetimes measured for the calcined samples at 900 °C are relatively high being comparable to those obtained for the europium doped phosphosilicate glasses [30]. It is generally known, that the thermal treatment of various lanthanides-exchanged micro/mesoporous materials induces lengthening of the PL decays due to water removal from the first coordination shell. In addition, calcination of the Eu–OSP1 and Eu–OSP2 materials leads to the removal of the reacted surfactant, modifying both the short- and long-range environments at the Eu sites as evidenced from the NMR, DR-UV/vis and PL spectra.

Table 2
Relevant photophysical properties of Eu–OSP1 and Eu–OSP2.

Sample	$\langle\tau\rangle$ (μs) (±5%)	A_{rad} (s^{-1})	η (%)
Dried Eu–OSP1	370		
Calcined Eu–OSP1 (450 °C)	540	300	16
Calcined Eu–OSP1 (900 °C)	1060	360	30

For the special case of the europium ion, the shape of the (corrected) emission spectrum is related to its radiative lifetime (and thus to the intrinsic quantum efficiency of emission, η) via the simple equation of Werts and co-authors [31].

$$\eta = \tau * A_{rad} = A_{01} * \tau * \frac{I_{tot}}{I_{01}} \quad (3)$$

where τ is the experimental lifetime, A_{rad} is the radiative relaxation rate, I_{tot} and I_{01} are the integrated area corresponding to the total emission spectrum and $^5D_0$–$^7F_1$ transition, respectively. A_{01} is the Einstein coefficient of spontaneous emission for the $^5D_0$–$^7F_1$ transition. Since A_{01vac} is 14.65 s^{-1} in vacuo and when an average refraction index n equal to 1.506 is considered, the value of $A_{01} = n^3(A_{01vac})$ is approx. 50 s^{-1} [32]. Due to subtle differences in the spectral properties of the Eu–OSP1 and Eu–OSP2, the quantum efficiency of emission and A_{rad} values can be regarded as similar within the experimental error and only the data for the Eu–OSP1 are listed in Table 2. The low luminescence quantum efficiency observed with the lanthanides-exchanged materials is generally related to the vibrational coupling to OH groups directly bound to Eu ions. From the comparison of the radiative relaxation rates at 450 and 900 °C, we can conclude that the decrease of the non-radiative relaxation rate due to OH removal is the main factor responsible for the increase by almost 100% of the average PL lifetime of europium (from 540 μs at 450 °C to 1060 μs at 900 °C).

4. Conclusions

Two mesoporous silicon-phosphate materials (OSP1 and OSP2) were synthesized by using two different groups of mixture surfactants, i.e. $(CH_3)3C_{13}H_{27}NBr$ with HO-PO(i-$C_3H_7)_2$ and $(CH_3)_3C_{13}H_{27}NBr$ with $(C_2H_5)_3(C_6H_5)PCl$ respectively, and subjected to ion-exchange with europium to obtain Eu–OSP1 and Eu–OSP2. All textural and PL data evidence a major contribution of the surfactant to the specific morphology of the solids. While the morphology of the OSP2 sample is more spherical, the structure of OSP1 obtained with a mixture of cationic and anionic surfactants corresponds to more compact solid and larger pores. ^{31}P and ^{29}Si CP/MAS NMR spectra indicate that these materials are amorphous with mesoporous properties in which the phosphorous is present as Q_0 or Q_1 unit. The PL properties of Eu–OSP1 and Eu–OSP2 were also drastically changed with the thermal treatment. While for the dried samples subtle differences between the radiative and non-radiative relaxation pathways were observed according to surfactant, following calcination the differences became negligible. Finally, a strong increase of the intrinsic quantum efficiency of europium emission was measured: from 16 to 30% in the calcined samples at 450 and 900 °C, respectively.

Acknowledgement

Author Carmen Tiseanu acknowledges the partial financial support from the national project grants LAPLAS- PN06 36 02 01 and CEEX 06 D11 53 2005.

Appendix A. Supplementary data

Supplementary data associated with this article can be found, in the online version, at doi:10.1016/j.jphotochem.2010.07.015.

References

[1] F. Hoffmann, M. Cornelius, J. Morell, M. Fröba, Angew. Chem. Int. Ed. 45 (2006) 3216–3251.
[2] N.K. Raman, M.T. Anderson, C.J. Brinker, J. Chem. Mater. 8 (1996) 1682–1701.
[3] C. Sanchez, B. Lebeau, F.-J. Chaput, P. Boilot, Adv. Mater. 15 (2003) 1969–1994.
[4] P. Escribano, B. Julián-López, J. Planelles-Aragó, E. Cordoncillo, B. Viana, C. Sanchez, J. Mater. Chem. 18 (2008) 23–40.
[5] R.J.P. Corriu, D. Leclercq, P.H. Mutin, L. Sarlin, A. Vioux, J. Mater. Chem. 8 (1998) 1827–1833.
[6] M.A. Markowitz, G. Deng, B.P. Gaber, Langmuir 16 (2000) 6148–6155.
[7] M.A. Markowitz, G. Deng, M.C. Burleigh, E.M. Wong, B.P. Gaber, Langmuir 17 (2001) 7085–7092.
[8] M. Jurado-Gonzalez, D. Li Ou, A.C. Sullivan, J.R.H. Wilson, J. Mater. Chem. 12 (2002) 3605–3609.
[9] A. Aliev, D. Li Ou, B. Ormsby, A.C.J. Sullivan, J. Mater. Chem. 10 (2000) 2758–2764.
[10] S. Santra, B. Liesenfeld, D. Dutta, D. Chatel, C.D. Batich, W. Tan, B.M. Moudgil, R.A. Mericle, J. Nanosci. Nanotechnol. 5 (2005) 899–904.
[11] H. Zhou, S. Xu, M. Ye, S. Feng, C. Pan, X. Jiang, X. Li, G. Han, Y. Fu, H. Zou, J. Proteome Res. 5 (2006) 2431–2437.
[12] M. Manzano, A.J. Salinas, M. Vallet-Regi, Prog. Solid State Chem. 34 (2006) 267–277.
[13] D.E.C. Corbridge, Phosphorus: An Outline of its Chemistry Biochemistry and Technology, Elsevier Science Publishers, Amsterdam, 1990.
[14] A.M. Modro, T.A. Modro, Can. J. Chem. 77 (1999) 890–894.
[15] A. Monnier, F. Schuth, Q. Huo, D. Kumar, D. Margolese, R.S. Maxwell, G.D. Stucky, M. Krishnamurty, P. Petroff, A. Firouzi, M. Janicke, B.F. Chmelka, Science (1993) 1299–1303.
[16] D. Massiot, F. Fayon, M. Kapron, I. King, S. Le Calve, B.-J. Alonso, O. Durand, B. Bujoli, Z. Gan, G. Hoatson, Magn. Reson. Chem. 40 (2002) 70–76.
[17] M. Feike, C. Jager, H.W. Spiess, J. Non-Cryst. Solids 223 (1998) 200–206.
[18] N.J. Clayden, P. Pernice, A. Aronne, J. Non-Cryst. Solids 351 (2005) 195–202.
[19] J.P. Osegovic, R.S. Drago, J. Catal. 182 (1999) 1–4.
[20] B. Chakraborty, A.C. Pulikottil, B. Viswanathan, Appl. Catal. A 167 (1998) 173–182.
[21] M. de la Fuente, Ć.A. Hernanz, Ć.R. Navarro, J. Biol. Inorg. Chem. 9 (2004) 973–986.
[22] I.N. Chakraborty, R.A. Condrate, Phys. Chem. Glasses 26 (1985) 68–73.
[23] G. Blasse, J. Chem. Phys. 45 (1966) 2356–2360.
[24] P. Dorenbos, J. Lumin. 111 (2005) 89–104.
[25] E.W.J.L. Oomen, A.M.A. van Dongen, J. Non-Cryst. Solids 111 (1989) 205–213.
[26] G. Blasse, A. Bril, Philips Res. Rep. 21 (1966) 368–378.
[27] R. Reisfeld, E. Zigansky, M. Gaft, Mol. Phys. 102 (2004) 1319–1330.
[28] M.J. Weber, Phys. Rev. 171 (1968) 283–291.
[29] C. Tiseanu, V.I. Parvulescu, M. Kumke, A. Gessner, J. Martens, J. Phys. Chem. B 112 (2008) 10552–10562.
[30] L.R. Avila, E.C. de, O. Nassor, P.F.S. Pereira, A. Cestari, K.J. Ciuffi, P.S. Calefi, E.J. Nassar, J. Non-Cryst. Solids 354 (2008) 4806–4810.
[31] H. Martinus, V. Werts, Y. Ronald, T.F. Jukes, J.W. Verhoeven, Phys. Chem. Chem. Phys. 4 (2002) 1542–1548.
[32] M.F. Hazenkamp, G. Blasse, Chem. Mater. 2 (1990) 105–110.